Stability of Brillouin flow in the presence of slow-wave structure

D. H. Simon,[1] Y. Y. Lau,[1] G. Greening,[1] P. Wong,[1] B. Hoff,[2] and R. M. Gilgenbach[1]
[1]*Department of Nuclear Engineering and Radiological Sciences, University of Michigan, Ann Arbor, Michigan 48109-2104, USA*
[2]*Air Force Research Laboratory, Kirtland Air Force Base, Albuquerque, New Mexico 87117, USA*

(Received 30 May 2016; accepted 9 August 2016; published online 2 September 2016)

Including a slow-wave structure (SWS) on the anode in the conventional, planar, and inverted magnetron, we systematically study the linear stability of Brillouin flow, which is the prevalent flow in crossed-field devices. The analytic treatment is fully relativistic and fully electromagnetic, and it incorporates the equilibrium density profile, flow profile, and electric field and magnetic field profiles in the linear stability analysis. Using parameters similar to the University of Michigan's recirculating planar magnetron, the numerical data show that the resonant interaction of the vacuum circuit mode and the corresponding smooth-bore diocotron-like mode is the dominant cause for instability. This resonant interaction is far more important than the intrinsic negative (positive) mass property of electrons in the inverted (conventional) magnetron geometry. It is absent in either the smooth-bore magnetron or under the electrostatic assumption, one or both of which was almost always adopted in prior analytical formulation. This resonant interaction severely restricts the wavenumber for instability to the narrow range in which the cold tube frequency of the SWS is within a few percent of the corresponding smooth bore diocotron-like mode in the Brillouin flow. *Published by AIP Publishing.* [http://dx.doi.org/10.1063/1.4961917]

I. INTRODUCTION

There are two models to describe the motion of an electron in the basic state of a magnetron. The first is the single particle orbit model,[1] and the second is the Brillouin flow model.[2] In the single particle model, an electron emitted from the cathode surface executes a cycloidal orbit before it returns to the cathode. In the Brillouin flow model, the electrons form a laminar shear flow, and each electron in the laminar flow travels parallel to the cathode surface. Slater[3] argued that the Brillouin flow is the prevalent state relative to the single particle cycloidal orbit. Particle-in-cell simulations[4–6] have since shown the predominance of the Brillouin flow, as predicted by Slater.[3] The Buneman-Hartree condition (BH), which is the operating condition for magnetrons, may also be derived from either the single particle cycloidal orbit model[7,8] or the Brillouin flow model.[9] The two BHs are different for cylindrical geometry.[9] It was also shown that the BH obtained from the Brillouin flow model provided a much better agreement for experiments and simulations of relativistic magnetrons than the traditional BH that was derived from the single particle orbit theory.[10] Thus, we provide here an in-depth analysis of Brillouin flow stability. The important inclusion is in the presence of a slow-wave structure (SWS). Our treatment is fully relativistic and fully electromagnetic.

There has been a long history of study of the stability of the Brillouin flow.[11–18] These studies were developed in an attempt to understand (a) magnetron startup and (b) noise generation mechanism. These two issues remain not well understood to this date. A major deficiency in these stability studies is that the slow-wave structure (SWS) on the anode circuit has been largely ignored, i.e., the stability analysis applies only to the smooth bore magnetron. This eliminates the entire class of synchronous interaction between electrons and the SWS. The underlying reason may easily be seen for a smooth bore planar magnetron, where the phase velocity of any vacuum mode along the direction of the electron flow is always larger than c (c = light speed in vacuum), whereas the electron speed is always less than c; so, synchronous interaction is impossible. Particle-in-cell simulations including slow wave structures are incapable of extracting small signal growth because of overmode and nonlinear behaviors, compounded by electrons generated and removed from the code, making growth of density perturbations due to a single mode impossible to determine.

Our recent stability analysis[18] of the Brillouin flow in a smooth bore magnetron shows that the diocotron-like instability in the shear flow is destabilized (stabilized) in the inverted magnetron (conventional magnetron) geometry. This is consistent with the expected negative mass (positive mass) behavior of a single electron in the inverted (conventional) magnetron which has the anode inside (outside) the cathode.[19–21] It is interesting that the negative mass effect on a thin electron layer[19,20] in the inverted magnetron configuration is not destroyed by the substantial velocity spread that is always present in the Brillouin flow. (Recall that the Brillouin flow velocity is zero on the cathode and rises to a maximum value at the top of the Brillouin hub, roughly in a linear fashion.[22,23]) This analytical result is also consistent with simulations of the recirculating planar magnetron which showed enhanced bunching in the cylindrical bends of the inverted magnetron configuration where there is no SWS in the circular bends.[24–26] However, these smooth bore magnetron studies could not explain why the widely deployed conventional magnetrons, which always have SWS, could have a fast startup despite the stabilizing positive mass effects.[19–21]

In this paper, we include a SWS in the anode. The SWS introduces possible resonance between the waves on the slow wave circuit and a class of electrons within the

Brillouin hub. This resonant interaction dominates over the negative/positive mass effect, and it becomes the main cause of the instability. Our data show that this resonant instability in a SWS conventional magnetron may even have a higher growth rate than the resonant instability in the SWS inverted magnetron. Contrary to the smooth bore magnetron, this resonant instability can occur only over a rather restricted range of wavenumber, in which the cold tube frequency of the SWS is close to the real part of the eigenfrequency for the Brillouin flow in the corresponding smooth bore magnetron.

This paper will include fully relativistic and fully electromagnetic formulation of the eigenvalue solutions for the linear stability of Brillouin flow in a SWS structure, in both planar magnetron (Fig. 1), and cylindrical conventional and inverted magnetrons (Fig. 6 below). The periodic boundary conditions that result from the SWS mean that solutions must now include space harmonics both in the vacuum region[27] and within the Brillouin flow.[10] The equilibrium density profile, flow profile, and DC electric and DC magnetic field profiles of the Brillouin flow[9,22,23] are used in the governing linearized equation for stability. This equation will be integrated for each space harmonic and matched with the vacuum field solution. The formulation and numerical results are presented in Section II for planar magnetron, using the parameters similar to our Recirculating Planar Magnetron (RPM) experiments.[26] The corresponding theory and numerical results for cylindrical conventional and inverted magnetrons are presented in Section III, using similar dynamical parameters as the planar SWS magnetron in Section II. Concluding remarks are given in Section IV.

II. PLANAR BRILLOUIN FLOW

The geometry for the system is shown in Figure 1. The cathode is located at $x=0$, and the anode is at $x=x_a$; the anode SWS has a period L, cavity width w_c, and cavity height h. The Brillouin flow is in the y-direction, extending from the cathode surface to $x=x_b$ (the $y=0$ axis is along the center line of a cavity), the DC gap voltage is V, and the external magnetic field (in vacuum) is B_0. The base case parameters are specified in the caption of Fig. 1. The dimensions of the SWS are based on the RPM-12a, which was tested at The University of Michigan.[26] The relativistic Brillouin flow equilibrium[15] is assumed to be the same as a smooth-bore anode. This assumption is justified by the boundary condition that requires the field to be normal to the cathode.[10] The non-uniformity of E_y caused by the periodic SWS is greatly reduced some distance below the anode.[10] We thus assume that the equilibrium Brillouin flow with the SWS is the same as the equilibrium Brillouin flow with a smooth-bore anode at $x = x_a$.[15]

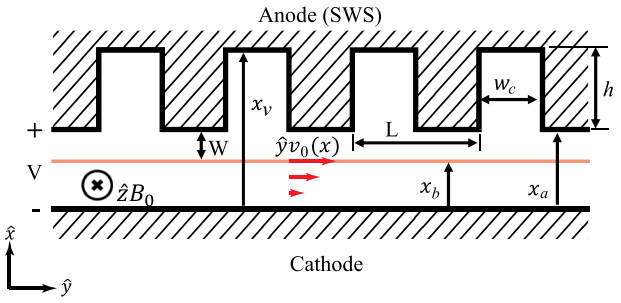

FIG. 1. Diagram of a planar magnetron with a slow wave structure. The base case parameters for stability analysis are: $x_a = 3.9$ cm, $x_b = 1.54$ cm, L = 3.84 cm, $w_c = 1.92$ cm, h = 6.31 cm, $B_0 = 0.0645$ T, and V = 300 kV.

The last assumption means that the governing equation for electron motion and the jump condition across the outermost layer of the Brillouin hub are the same as those presented in Ref. 28 for the smooth-bore anode,[18] for each of the space harmonics of the RF field $\vec{E}$ (which now contains space harmonics[27]), both within the Brillouin flow and in the vacuum region. These space harmonics must be matched to the perturbations within the Brillouin flow. The vacuum fields in these geometries have been derived in the literature,[27,29] so they will be presented with minimal derivation. The periodic vacuum fields have, according to the Floquet theorem,[27] the form given below, for $x_b < x < x_a$ (Figure 1),

$$\boldsymbol{E} = \sum_{n=-\infty}^{\infty} (\hat{x}E_{xn}(x) + \hat{y}E_{yn}(x))e^{j(\omega t - k_n y)}, \tag{1}$$

$$\boldsymbol{H} = \sum_{n=-\infty}^{\infty} \hat{z}H_{zn}(x)e^{j(\omega t - k_n y)}, \tag{2}$$

$$k_n = k_0 + 2\pi n/L, \tag{3}$$

where $n = 0, \pm1, \pm2, \ldots$. Each value of n corresponds to a space harmonic. Solving Maxwell's equations within the vacuum region, $x_b < x < x_a$ gives the form of each of these fields

$$H_{zn}(x) = B_n \cosh(\mathrm{s_n}(x - x_a)) + C_n \sinh(s_n(x - x_a)), \tag{4}$$

$$E_{xn}(x) = -\frac{k_n}{\omega\epsilon_0}\left[B_n \cosh(\mathrm{s_n}(x - x_a)) + C_n \sinh(s_n(x - x_a))\right], \tag{5}$$

$$E_{yn}(x) = -\frac{s_n}{j\omega\epsilon_0}\left[B_n \sinh(\mathrm{s_n}(x - x_a)) + C_n \cosh(s_n(x - x_a))\right], \tag{6}$$

where $s_n = (k_n^2 - \omega^2/c^2)^{1/2}$, and C_n and B_n are constants.

We assume a TEM mode within the cavities, $x_a < x < x_v$, as was done in Refs. 27, 30, and 31, so the field over one period (L) is given by

$$E_y(x,y) = \begin{cases} D\sin\left(\dfrac{\omega}{c}(x - x_v)\right), -\dfrac{w_c}{2} < y < \dfrac{w_c}{2} \\ 0, \ otherwise, \end{cases} \tag{7}$$

$$E_x(x) = 0, \tag{8}$$

$$H_z(x) = j\left(\frac{\epsilon_0}{\mu_0}\right)^{1/2} D\cos\left(\frac{\omega}{c}(x - x_v)\right), \tag{9}$$

where D is a constant. The boundary condition that E_y be continuous at the cavity mouth ($x = x_a$, $-L/2 < y < L/2$) is then given by

$$\frac{1}{j\epsilon_0\omega}\sum_{n=-\infty}^{\infty} s_n C_n e^{-jk_n y} = \begin{cases} D\sin\left(\frac{\omega h}{c}\right), & \frac{-w_c}{2} < y < \frac{w_c}{2} \\ 0, & \frac{w_c}{2} < |y| < \frac{L}{2}, \end{cases} \tag{10}$$

where $h = x_v - x_a$. This equation is a Fourier series, so solving for the coefficients produces

$$C_n = j\omega\epsilon_0 \frac{D}{s_n}\frac{w_C}{L}\sin\left(\frac{\omega h}{c}\right)\frac{\sin(\theta_n)}{\theta_n}, \tag{11}$$

where $\theta_n = k_n w_c/2$. The second boundary condition is that the average magnetic field over the cavity mouth is continuous. This boundary condition becomes

$$j\left(\frac{\epsilon_0}{\mu_0}\right)^{1/2} D\cos\left(\frac{\omega h}{c}\right) = \frac{1}{w_c}\int_{-w_c/2}^{w_c/2}\left(\sum_{n=-\infty}^{\infty} B_n e^{-jk_n y}\right)dy. \tag{12}$$

After performing the integration and moving the term D into the sum (since it is constant), Eq. (12) becomes

$$j\left(\frac{\epsilon_0}{\mu_0}\right)^{1/2}\cos\left(\frac{\omega h}{c}\right) = \sum_{n=-\infty}^{\infty}\frac{B_n}{D}\frac{\sin(\theta_n)}{\theta_n}. \tag{13}$$

Equation (11) can be solved for D, which is substituted into Eq. (13) to get the final vacuum boundary equation

$$1 - \frac{\omega}{c}\tan\left(\frac{\omega h}{c}\right)\frac{w_c}{L}\sum_{n=-\infty}^{\infty}\frac{1}{s_n}\frac{B_n}{C_n}\left(\frac{\sin\theta_n}{\theta_n}\right)^2 = 0. \tag{14}$$

The ratio of B_n/C_n is still needed in order to solve Eq. (14). In order to find this value, we must make the assumption that each vacuum space harmonic creates a corresponding mode within the Brillouin hub. For each wavenumber k_n, the value for the ratio of $\phi_n'(x_b)/\phi_n(x_b)$ from the numerical solution (where ϕ_n is a perturbation quantity) within the Brillouin flow (taking into account the jump condition at $x = x_b$) is set equal to the ratio of $\phi_n'(x_b)/\phi_n(x_b)$ of the vacuum field at $x = x_b$. The hub potential, ϕ, is essentially the tangential electric field, E_y. This boundary condition was also used in the derivation of the dispersion relation for thin beams in SWS, in which each space harmonic creates a corresponding density and current perturbation in the linear theory.[30,31]

The value for the hub potential within the Brillouin hub for each space harmonic must be numerically integrated from the governing eigenvalue equation, which is derived in Ref. 28 as Eq. (93). The jump condition is found by integrating the eigenvalue equation across the edge of the Brillouin flow, described (but not shown explicitly) in Ref. 28, and is given by Eq. (4) of Ref. 18 for electrostatic modes.

The jump condition will be given for the cylindrical Brillouin flow in the Appendix. Together with the jump condition, the hub potential just outside the Brillouin hub is matched to the vacuum solution (Eq. (6))

$$\frac{\phi_n'(x_b)}{\phi_n(x_b)} = s_n\frac{[B_n\cosh s_n W + C_n\sinh s_n W]}{[B_n\sinh s_n W + C_n\cosh s_n W]}, \tag{15}$$

where $W = x_a - x_b$ and the left side of the equation is known from integrating over the Brillouin flow, incorporating the jump condition as explained in the preceding paragraph. Equation (15) can be rearranged to find B_n/C_n

$$\frac{B_n}{C_n} = \frac{\sinh(s_n W) - \frac{\phi_n'(x_b)}{s_n\phi_n(x_b)}\cosh(s_n W)}{\frac{\phi_n'(x_b)}{s_n\phi_n(x_b)}\sinh(s_n W) - \cosh(s_n W)}, \tag{16}$$

which can be used to solve Eq. (14). Equation (14) then becomes the hot tube dispersion relation. It contains an infinite sum, which has been tested empirically for different numbers of terms and shows almost no variation in solutions for $|n| \geq 4$ (9 terms). The results presented in this paper will use up to $|n| = 5$.

In the limit that the Brillouin hub height approaches the cathode, ϕ_{n1} approaches zero. In this limit, B_n/C_n simply becomes $-\coth(s_n x_a)$, and Eq. (14) reduces to the cold-tube dispersion relation of the SWS.[27]

Solutions to Eq. (14) as a function of wavenumber will be presented in this section, while additional parameter sweeps[10] will be discussed. In addition, it will be argued that the diocotron-like instability found in the planar smooth-bore magnetrons interacts with the resonant mode created by the SWS circuit, and that this interaction explains the shape of the parameter sweeps. More specifically, it will be shown that the maximum growth occurs when the real part of the frequency of the diocotron-like instability (in the corresponding smooth-bore geometry) and the SWS cold tube frequency are almost equal, and that the system stabilizes as these two frequencies diverge. To this end, the smooth-bore anode solutions to the same geometry (without the cavities) and operating parameters will be presented. The eigenvalue frequency is written as $\omega = \omega_r - i\omega_i$ so that ω_i is the growth rate. The hot tube SWS eigenvalue solutions will be referred to as $\omega_{sws} = \omega_r^{sws} - i\omega_i^{sws}$, the hot tube smooth-bore eigenvalue as $\omega_{sb} = \omega_r^{sb} - i\omega_i^{sb}$, and the cold tube frequency of the SWS will be ω_{ct}. *We shall show that instability occurs only when* $\omega_r^{sws} \approx \omega_r^{sb} \approx \omega_{ct}$.

The base geometry has the dimensions of the planar section of the RPM-12a:[26] an Anode-Cathode (AK) gap width $x_a = 3.9$ cm, a period L = 3.84 cm, a vane width $w_c = L/2$, equal to half the period, and a vane height of $h = 6.31$ cm (see also Fig. 1). The operating conditions have been chosen so that the eigenvalue solution to the base case has an imaginary component at the fixed π-mode ($k_0 = \pi/L$) which is the usual operating mode in a SWS magnetron, where the RF fields change sign in adjacent cavities. The operating conditions are 0.0645 T and 300 keV, which put the Brillouin hub height at $x_b = 1.54$ cm, about half of the AK gap width x_a. The base case is operated in π-mode, which corresponds to $k_0 = 81.8$ rad/m. For this section, π-mode will refer to the wavenumber (or azimuthal mode number, for the cylindrical magnetrons) at which there is a π phase shift in the electric

field between adjacent cavities, and not the cold tube frequency that corresponds to this shift. At these parameters, $\omega_i^{sws}/\omega_r^{sws}$ is ~3%, which is on the order of the peak value for the instability growth rate for the parameter sweeps that will be presented in this section. The cold tube dispersion relation is shown in black in Figure 2, along with the line representing the maximum electron frequency (in red) in the Brillouin hub (defined as $\omega_e(k) \equiv v_0(x_b) * k_0$) and the real part of the eigenvalue solution ($\omega_r^{sws} = 6.51 \times 10^9$ rad/s at the π-mode).

The base case has π-mode operation ($k_0 = 81.8$ rad/m). The real part of the hot tube frequency is found to be linear with wavenumber, represented by the solid blue line in Figure 3, which shows the parameter sweep in the wavenumber k_0. The imaginary part (i.e., the growth rate) shows a symmetric profile around a central peak of 80 rad/m as shown in the solid green curve in Figure 3. It extends for 4% of the wavenumber at peak growth in either direction before stabilizing. Wavenumbers k_0 from 30 to 90 rad/m were tested; only those plotted in Figure 3 showed growth with the SWS anode. This includes the intersection of ω_e and ω_{ct} at $k_0 = 38$ rad/m shown in Figure 2. The smooth-bore anode shows no growth in this region, as shown in the dashed green line in Fig. 3.

Figure 2 shows that there is always an electron layer within the Brillouin hub that is synchronous with the RF in the cold tube for all wavenumbers larger than the intersection point at 38 rad/m (Figure 2), and yet Figure 3 shows that synchronism only produces growth for the range of wavenumbers between 77 and 83 rad/m. A comparison of ω_r for the smooth-bore and ω_{ct} shows that very close to the point at which they intersect each other ω_i for the SWS is at a maximum. The true maximum peak for ω_i for the SWS occurs at 80 rad/m, while the intersection of ω_r for the smooth-bore and cold tube occurs at 80.2 rad/m. ω_r for the SWS lies between the smooth-bore and cold tube values, and is very close to the average value of two ($\omega_r(average) = \omega_{ct}/2 + \omega_r^{sb}/2$). This relation, where ω_r^{sws} is the average of ω_{ct} and ω_r^{sb}, will hold true for π-mode results, but not for the results at other modes, as will be shown in Figure 4. As ω_{ct} and ω_r^{sb} diverge, the hot tube growth rate in the SWS, ω_i^{sws}, decreases. When the difference between ω_{ct} and ω_r^{sb} exceeds about 4%, $\omega_i^{sws} \to 0$, and the system becomes stable. This strongly suggests that the SWS resonantly excites the diocotron instability in the Brillouin flow. This synchronous instability is absent in the corresponding smooth-bore magnetron under the electrostatic approximation.

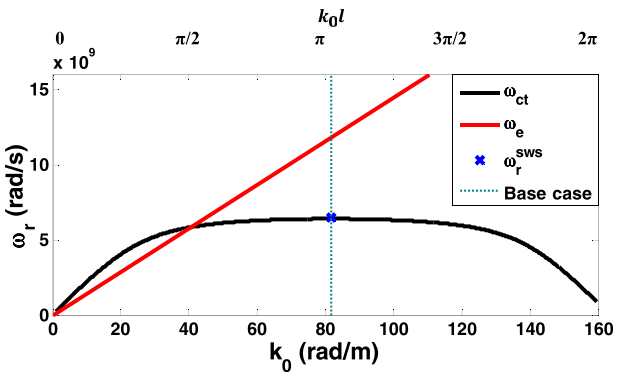

FIG. 2. Base case ($k_0 = 81.8$ rad/m corresponding to π-mode) plot of cold tube dispersion relation (ω_{ct}), beam line with maximum velocity (ω_e), and value for the real part of ω from the eigenvalue solution (ω_r^{sws}).

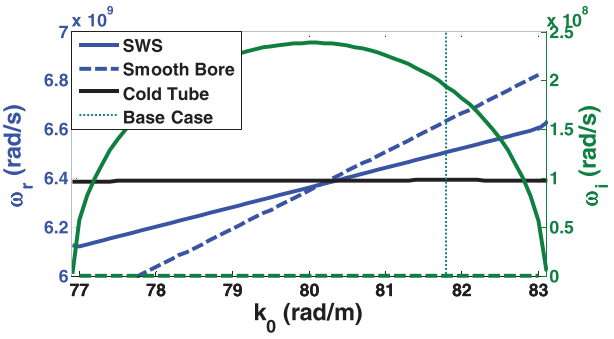

FIG. 3. Eigenvalue solutions for ω_r and ω_i as a function of k_0, with all other parameters equal to the base case (shown as the vertical dotted line). Solid lines correspond to SWS and dashed lines to smooth-bore.

Additional parameter sweeps were performed, which include varying voltage and magnetic field while keeping the Brillouin hub height constant, varying voltage and Brillouin hub height while keeping magnetic field constant, and changing the cavity depth x_v. The three main trends that are common to all sweeps are (a) that the maximum growth rate occurs very close to (although not exactly at) the point at which ω_{ct} and ω_r^{sb} intersect, (b) that ω_r^{sws} is nearly the average of ω_{ct} and ω_r^{sb}, and (c) that a small difference (up to ~8%) in ω_{ct} and ω_r^{sb} leads to stabilization of the system.

Figure 4 shows a sweep of wavenumber for $x_b = 2.5$ cm; this hub height is obtained by raising the gap voltage, but fixing the magnetic field and all other parameters equal to the base case. Figure 4 has two regions of instability for the SWS magnetron (solid green line). The first one, for 27 rad/m $< k_0 <$ 57 rad/m, follows the same three trends as the sweeps of wavenumber. Sweeps in cavity height and magnetic field also show the same trend.[10] The second region of instability (Fig. 4) occurs when the wavenumber exceeds 70 rad/m. The start of this instability roughly coincides with the start of instability growth in the smooth-bore magnetron ($k_o >$ 65 rad/m). The instability is an order of magnitude lower than the peak instability growth rate at $k_0 = 45$ rad/m and continues to a wavenumber of about 90 rad/m. The second instability differs from the first in a number of ways. The growth for the second instability occurs in a region in which ω_{ct} (black curve) and ω_r^{sb} (dashed blue curve) differ

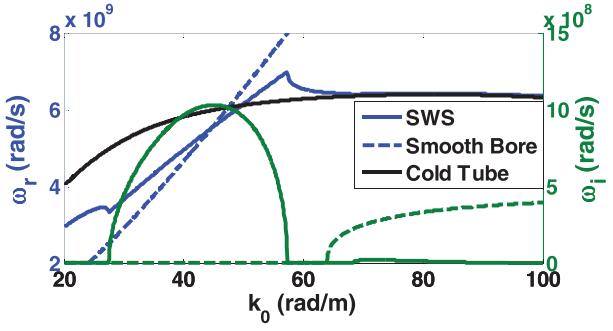

FIG. 4. Eigenvalue solutions for ω_r and ω_i as a function of k_0 for $x_b = 0.025$ m, by raising the gap voltage, with all other parameters equal to the base case.

by a factor of ∼2, whereas these frequencies are roughly equal for the first instability. In the first instability, ω_r^{sws} (solid blue curve) is nearly the average of ω_{ct} (black curve) and ω_r^{sb} (dashed blue curve), while in the second instability, ω_r^{sws} is just slightly higher than ω_{ct} and does not appear to be influenced by ω_r^{sb}. This suggests that the second instability represents a mild destabilization of the cold tube mode by the diocotron effect. Note that at $k_0 \approx 45$ rad/m, $\omega_i^{sws}/\omega_r^{sws} \approx 20\%$, implying a very high growth rate. This high growth rate is probably due to much larger hub height x_b, making the fringing field at the vane more appreciable at the synchronous electron layer.

Figure 5 has a separation of the strong instability in the SWS and the onset of instability in the smooth-bore magnetron. This separation is a result of the geometry chosen, and it is instructive to change the geometry to such an extent that both the SWS and smooth-bore magnetrons are unstable at the same operating parameters and wavenumbers. Figure 5 shows a sweep of h at $x_b = 0.025$ m and π-mode. The smooth-bore magnetron is unstable in this figure as shown by the dashed green line. The cold tube frequency of the SWS magnetron (black line) is changed as h is changed, leading to a region where the SWS magnetron experiences the strong instability ($h < 0.032$ m). The weaker instability region ($0.04\,\text{m} < h < 0.08\,\text{m}$) is also present here. There is no smooth transition of the weak instability region to the strong instability region, as shown in Figure 5. When ω_{ct} approaches ω_r^{sb}, the synchronous instability starts, and its growth rate is ∼3 times larger than the diocotron-like only instability present in the smooth-bore magnetron.

The results presented in this section support the argument made at the beginning that the strong instability is a result of an interaction between the layer of electrons subject to the diocotron-like instability and the resonance caused by the SWS. The figures show close agreement between the cold tube and smooth-bore frequencies in the regions in which the SWS magnetron is unstable. In general (although there is a small exception in Figure 4), the SWS unstable mode's frequency lies between the cold tube and smooth-bore frequencies.

The weak instability behaves differently. It appears to coincide with the start of the diocotron-like instability in the smooth-bore magnetron; however, it occurs very near the cold tube frequency and quite far from the smooth-bore diocotron frequency. Also of interest is there is no smooth transition between this weak instability and the strong synchronous instability.

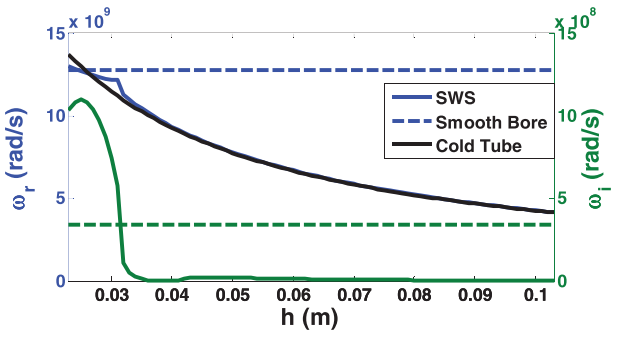

FIG. 5. Eigenvalue solutions for ω_r and ω_i at π-mode as a function of h at $x_b = 2.5$ cm, by raising the gap voltage, but fixing the magnetic field and all other parameters equal to the base case. Solid lines correspond to SWS and dashed lines to smooth-bore.

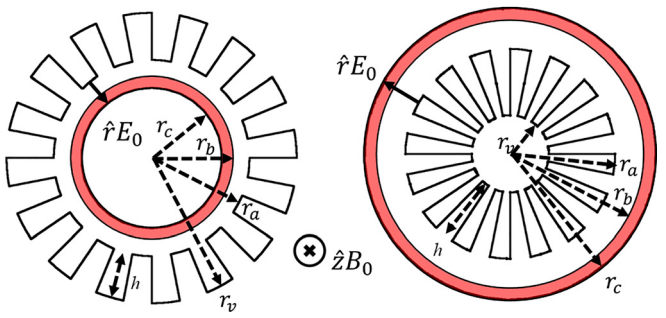

FIG. 6. Geometry of conventional (left) and inverted (right) cylindrical magnetrons. Graphs are not drawn to scale but are proportionally correct for the base case.

III. CYLINDRICAL BRILLOUIN FLOW

The basic geometry of the cylindrical magnetron with SWS is shown in Figure 6 for the conventional (left) and inverted magnetron (right). The Brillouin flow region is marked in red. In the conventional (inverted) magnetron, the cathode is on the inside (outside) and the anode is on the outside (inside). The base geometry of the cylindrical magnetron is similar to the planar section of the RPM-12a that was presented in Section II. This design was chosen so that a comparison could be made between the planar, conventional, and inverted magnetrons. The parameters of the base geometry are listed in Table I. The parameters that are common to the base case of all three geometries (planar, conventional, and inverted) are given in bold in Table I.

For the base case of the cylindrical magnetron, the inner radius (r_c for the conventional, r_a for the inverted) is 10 cm and the outer radius is 13.9 cm, resulting in an AK gap of 3.9 cm which is the same as the planar geometry. The cavity height h is 6.31 cm, so r_v is 20.21 cm for the conventional magnetron and 3.69 cm for the inverted. We assume that there are N = 16 cavities in both designs, and the π-mode has an azimuthal mode number $l = 8$. The number of cavities is chosen to keep the distance traveled by an electron over one

TABLE I. Operational parameters and geometry for the base case conventional and inverted magnetrons. Quantities that are the same between the two types and the planar magnetron are highlighted in bold.

Parameter	Conventional	Inverted
Cathode radius: r_c	10 cm	13.9 cm
Anode radius: r_a	13.9 cm	10 cm
AK gap: $\lvert r_c - r_a \rvert$	**3.9 cm**	**3.9 cm**
Brillouin hub: $\lvert r_b - r_c \rvert$	**1.54 cm**	**1.54 cm**
h : $\lvert r_v - r_a \rvert$	**6.31 cm**	**6.31 cm**
Magnetic field: B_0	**0.0645 T**	**0.0645 T**
Applied voltage: V	238 kV	378 kV
Number of cavities: N	16	16

period roughly equal to the planar period of L = 3.84 cm. The magnetic field is held constant at 0.0645 T, which results in a voltage of 238 kV for the conventional magnetron and 378 kV for the inverted magnetron (Table I).

As in Section II, the procedure for deriving the hot tube dispersion relation for the cylindrical magnetrons is the same as the planar geometry. For the cylindrical geometry (Figure 6), the small signal RF fields in between r_b and r_a are given by, assuming $e^{j\omega t - jn\theta}$ dependence,

$$H_{zn}(r,\theta) = B_n J_n(pr) + C_n Y_n(pr), \tag{17}$$

$$E_{rn}(r,\theta) = \left(-\frac{\omega\mu_0}{p^2}\frac{\mathrm{n}}{r}\right)\left[B_n J_n(pr) + C_n Y_n(pr)\right], \tag{18}$$

$$E_{\theta n}(r,\theta) = \left(\frac{j\omega\mu_0}{p}\right)\left[B_n J_n'(pr) + C_n Y_n'(pr)\right], \tag{19}$$

where $p = \omega/c$, and the prime denotes differentiation of the standard Bessel functions J_n and Y_n with respect to their argument. The azimuthal electric field in each vane entrance ($r = r_a$) is assumed to be constant, D, so that the RF fields within the vane (r between r_a and r_v) are given by

$$E_\theta(r,\theta) = \begin{cases} D\left[\dfrac{J_0'(pr)Y_0'(pr_v) - J_0'(pr_v)Y_0'(pr)}{J_0'(pr_a)Y_0'(pr_v) - J_0'(pr_v)Y_0'(pr_a)}\right]e^{-j2ql\pi/N}, & \dfrac{2q\pi}{N} - \theta_0 < \theta < \dfrac{2q\pi}{N} + \theta_0 \\ 0, \quad otherwise \end{cases}, \tag{20}$$

$$E_r(r,\theta) = 0, \tag{21}$$

$$H_z(r,\theta) = \frac{pD}{j\omega\mu_0}\left[\frac{J_0(pr)Y_0'(pr_v) - J_0'(pr_v)Y_0(pr)}{J_0'(pr_a)Y_0'(pr_v) - J_0'(pr_v)Y_0'(pr_a)}\right]e^{-j2ql\pi/N}, \tag{22}$$

where Eq. (20) applies to the qth cavity entrance which subtended an azimuthal angle $2\theta_0$,[31] $q = 1, 2, \ldots N$, and N is the number of cavities. The boundary conditions at the vane entrance are that the azimuthal electric field is matched exactly, and that only the average magnetic field is matched. As with the planar case, the first boundary condition leads to a set of Fourier coefficients

$$D\left(\frac{N\theta_0}{\pi}\right)\left(\frac{\sin(n\theta_0)}{n\theta_0}\right) = \left(\frac{j\omega\mu_0}{p}\right)\left[B_n J_n'(pr_a) + C_n Y_n'(pr_a)\right], \tag{23}$$

where the periodicity of the electric field in the vanes means that the values of n can be restricted to $n = l + mN$, where $l = 0, 1, 2, \ldots, N-1$, and m can be any integer including zero. The $l = 0$ mode is called the zero-mode (or 2π-mode), meaning that there is no (or 2π) phase shift between the neighboring cavities in the RF fields. The $l = N/2$ mode is called the π-mode. For each l, the $m = 0$ mode is called the fundamental mode, and other values of m are known as the m th space harmonic. The average magnetic field boundary condition leads to[31]

$$\frac{pDe^{-\frac{jq2l\pi}{N}}}{j\omega\mu_0}F = \frac{1}{2\theta_0}\sum_{\mathrm{m}=-\infty}^{\infty}\left[B_n J_n(pr_a) + C_n Y_n(pr_a)\right] \times \frac{2\sin(n\theta_0)}{n}e^{-\frac{j2q\pi n}{N}}, \tag{24}$$

where

$$F = \frac{J_0(pr_a)Y_0'(pr_v) - J_0'(pr_v)Y_0(pr_a)}{J_0'(pr_a)Y_0'(pr_v) - J_0'(pr_v)Y_0'(pr_a)}. \tag{25}$$

The exponents on both sides of Eq. (24) cancel exactly because they differ by $e^{-j2qmN\pi}$, which is unity, as q, m, and N are integers. Dividing Eq. (24) by D, and using Eq. (23) for D, results in a final equation

$$F - \frac{N\theta_0}{\pi}\sum_{\mathrm{m}=-\infty}^{\infty}\frac{\left[J_n(pr_a) + \dfrac{C_n}{B_n}Y_n(pr_a)\right]}{\left[J_n'(pr_a) + \dfrac{C_n}{B_n}Y_n'(pr_a)\right]}\left(\frac{\sin(n\theta_0)}{n\theta_0}\right)^2 = 0. \tag{26}$$

We use Eq. (14) of Ref. 19 to numerically integrate the solution $\phi_{n1}'(r_b)/\phi_{n1}(r_b)$ within the Brillouin flow for each space harmonic, where ϕ_{nl} is the eigenfunction proportional to the RF azimuthal electric field. We apply the jump condition, given in the Appendix, across the top of the Brillouin hub, $r = r_b$ (Figure 6). We may define a normalized impedance, b_n, in terms of this numerically integrated value of $\phi_{n1}'(r_b)/\phi_{n1}(r_b)$ (plus the jump condition) as

$$b_n = \left.\frac{iE_{rn}}{E_{\theta r}}\right|_{r_{vac}} = -\left.\frac{nr_b}{p^2r_b^2 - n^2}\frac{\phi_{n1}'(r_b)}{\phi_{n1}(r_b)}\right|_{r_{vac}}, \tag{27}$$

which is numerically obtained using the procedure outlined in the Appendix. Equation (27) must be equated to the normalized impedance obtained from the vacuum field solution at $r = r_b$, for each space harmonic

$$b_n = -\frac{n}{pr_b}\left(\frac{B_n J_n(pr_b) + C_n Y_n(pr_b)}{B_n J_n'(pr_b) + C_n Y_n'(pr_b)}\right). \tag{28}$$

From Eq. (28), the ratio C_n/B_n is given by

$$\frac{C_n}{B_n} = -\frac{\frac{b_n r_b p}{n} J_n'(pr_b) + J_n(pr_b)}{\frac{b_n r_b p}{n} Y_n'(pr_b) + Y_n(pr_b)}. \tag{29}$$

Upon substituting Eq. (29) into (26), with the understanding that b_n in Eq. (29) is now given in terms of the numerically integrated value of $\phi_{n1}'(r_b)/\phi_{n1}(r_b)$ (plus the jump condition) defined in (27), Eq. (26) is the hot tube dispersion relation. As with the planar case, in the limit that the Brillouin hub approaches the cathode, $r_b \to r_c$, $E_\theta \to 0$, and $b_n \to \infty$ by Eq. (27). Thus, $C_n/B_n \to -J_n'(pr_b)/Y_n'(pr_b) \cong -J_n'(pr_c)/Y_n'(pr_c)$ by Eq. (29), and the hot tube dispersion relation (26) then reduces to the traditional cold tube dispersion relation for the cylindrical magnetron.[29,31]

This section will cover the solutions to Eq. (26) for both the conventional and inverted magnetrons. The parameter sweeps will focus on the azimuthal mode number l, although the sweeps of magnetic field B, Brillouin hub height $|r_b - r_c|$, and vane height $h = |r_v - r_a|$, analogous to parameters discussed in the planar flow section (i.e., k_0, B, x_b, h) have also been performed.[10] In addition, the effect of curvature on the magnetic field sweep will be explored by changing the inner and outer radii and cavity number while keeping the AK gap and the distance traveled by an electron over one period (L = 3.84 cm) approximately constant.

In this section, it will be argued that the cylindrical Brillouin flow in a magnetron with a SWS is unstable when $\omega_r^{sws} \approx \omega_r^{sb} \approx \omega_{ct}$. This is the same instability condition as the Brillouin flow in a planar SWS magnetron. Furthermore, the peak normalized growth rate (ω_i/ω_r) does not appear to be influenced by the negative mass effect, as it is similar for both the conventional and inverted magnetrons (with the conventional magnetron showing slightly larger growth). The synchronous instability appears to be the dominant cause of instability growth, although curvature does have an effect on the range of unstable parameters and the overall magnitude of their instability.

Figure 7 shows the dispersion relation for the conventional (a) and inverted (b) magnetrons along with the base case beam lines and the eigenvalue solutions for each mode at the base case parameters (Table I). The maximum electron frequency within the Brillouin hub is now defined as $\omega_e(l) \equiv v_0(r_b) * l/r_b$. The inverted magnetron operates at a higher frequency than the conventional magnetron for a given mode number. The cavities conform to the cylindrical coordinate system, as shown in Figure 6, so the conventional magnetron has a greater RF path length for the same h value than the inverted magnetron.

The eigenvalue solutions in Figure 7 are at discrete points, since the azimuthal mode number, l, must be an integer. The hollow circular points represent the hot tube SWS solutions, while the plus signs represent the hot tube smooth-bore solutions. The solid circles are the result of the solutions overlapping. Both the conventional and inverted magnetrons show instability at the mode number where ω_r^{sb} is closest to ω_{ct}. This instability has a normalized growth rate (ω_i/ω_r) of 3.6% for the conventional magnetron and 2.2% for the inverted magnetron. In contrast, the peak ω_i/ω_r values for the

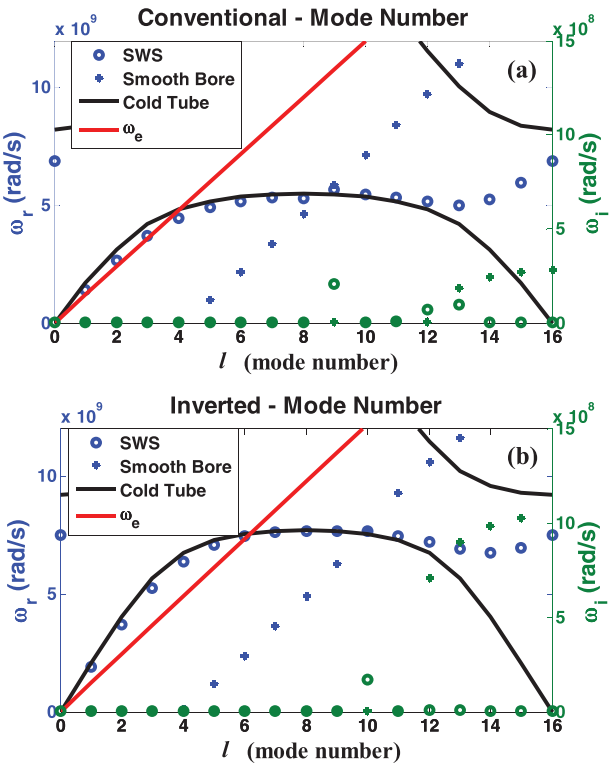

FIG. 7. Eigenvalue and cold tube solutions, along with the beam line ω_e, for (a) conventional and (b) inverted cylindrical magnetron for ω_r and ω_i as a function of l, with all other parameters equal to the base case. Circular markers correspond to SWS, plus sign markers to smooth-bore. The filled circles are intersections of the empty circles and the plus sign markers and indicate that the SWS and smooth-bore frequencies are the same for that mode.

smooth-bore magnetrons are 2.1% and 7.7%, respectively. Also of note, ω_r^{sb} is approximately 5×10^9 rad/s below ω_e, which is quite similar to the non-relativistic planar asymptotic formulation that predicts a difference of $0.55 * \omega_c$.[11] Here, $\omega_c(r) \equiv eB(r)/m\gamma(r)$, which is a constant 1.03×10^{10} rad/s for relativistic planar Brillouin flow, and varies by less than 2% over the Brillion hub in the cylindrical base cases.

The conventional magnetron (Fig. 7(a)) has a few l modes with lower growth rate at the point at which ω_r^{sb} intersects the second frequency band of the cold tube around $l = 12, 13$, although the inverted magnetron (Fig. 7(b)) shows no such growth at that point. At high mode numbers ($l > 11$), both magnetrons show a transition in ω_r^{sws} from the first frequency band of the cold tube to the second. This is coincident with the onset of instability in the smooth-bore magnetron, although it does not appear to cause additional instability growth for either SWS magnetron. One possible explanation for this behavior is that if ω_r^{sws} were to follow ω_{ct} in the high mode number region as ω_{ct} returns to 0 ($11 < l \leq 16$), then the synchronous layer would approach the cathode and be shielded from the interaction region by the bulk of the Brillouin flow. The general behavior follows the three main trends identified for the planar geometry and featured in the analogous planar wavenumber sweep.

An examination of the maximum normalized growth rates between the conventional and inverted magnetrons suggests that the conventional magnetron has a slightly higher normalized maximum growth rate (not shown). The values

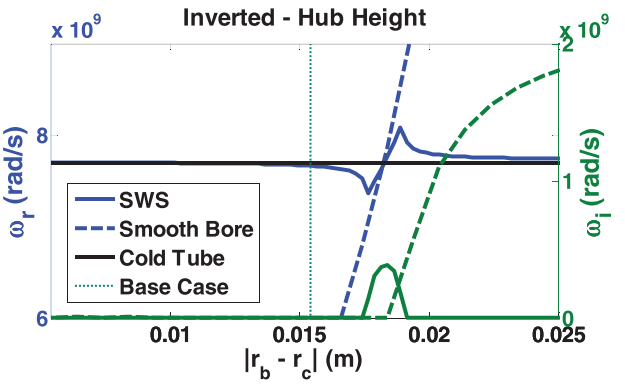

FIG. 8. Eigenvalue and cold tube solutions for an inverted cylindrical magnetron for ω_r and ω_i as a function of r_b, adjusting the voltage to keep a constant B, with all other parameters equal to the base case.

of ω_i^{sws} for the conventional and inverted magnetrons are actually closer than the normalized growth rates. With the data presented here, it is not possible to determine if the inverted SWS magnetrons are inherently more stable than their conventional counterparts. However, it is clear that the negative mass effect, which is held responsible for the peak $\omega_i^{sb}/\omega_r^{sb}$ (green crosses/blue circles in Figures 7(a) and 7(b)) for the inverted magnetron being over three times larger than the conventional magnetron in Figure 7, is not having the same effect in the presence of a SWS. Figure 8 shows that the instability growth of the SWS magnetron (solid green line), which is attributed to synchronous interaction with the SWS circuit, does not appear to be influenced by the instability growth due to the negative mass effect in the smooth-bore magnetron (dashed green line), despite having the same Brillouin flow profile.

Figure 9 shows the final sweep of magnetic field for different inner radii of the AK gap. The inner and outer radii of the AK gap (the anode and cathode) are changed in tandem, keeping the AK gap separation constant. The gap voltage is also changed so that the Brillouin hub height $|r_b - r_c|$ is constant. In addition, the number of cavities scales with the inner radius, to keep the electron path length over one period roughly a constant (for $r_{inner} = 10$, 15, 20 cm, $N = 16, 24, 32$). Both the conventional and inverted magnetrons show a trend toward smaller normalized growth rate peaks at lower magnetic fields as the inner radius is increased. The planar data is included here for comparison. The cylindrical magnetrons show a clear trend toward the planar magnetron as the inner radius increases, bringing the geometry closer to planar.

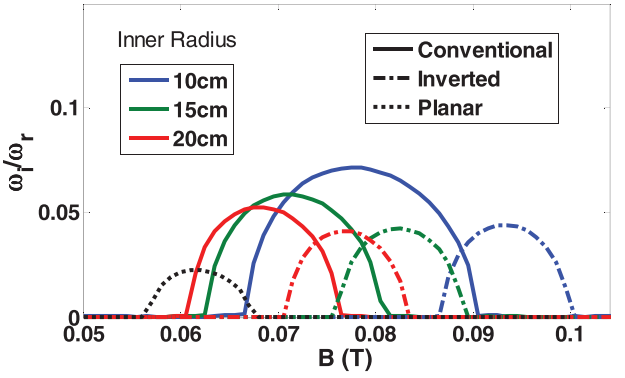

FIG. 9. Normalized growth rate as a function of magnet field (B) at π-mode for conventional cylindrical (solid), inverted cylindrical (dashed-dot), and planar (dot) magnetrons. The voltage is adjusted to keep a constant hub width $|r_b - r_c|$. The inner and outer radii are also changed to keep a constant AK gap constant, and the number of cavities is changed to keep the electron path length per period roughly constant.

IV. CONCLUDING REMARKS

Instability growth rates on the equilibrium Brillouin flow in a magnetron with a SWS anode are presented here for the first time. Analysis of the planar magnetron shows that instability growth is at its strongest when the real part of the frequency of the diocotron instability in the corresponding smooth-bore magnetron and the cold tube resonant frequency of the SWS has almost the same value. The instability vanishes as these two frequencies diverge, which means that the range of instabilities is relatively narrow. At the π-mode, most parameters can only be varied $\pm 8\%$ from their value at the peak of instability growth before the system stabilizes.

The cylindrical magnetrons are investigated next, and they show the same trends as the planar magnetron, although they exhibit a larger normalized growth rate for similar operational parameters. A comparison between the conventional and inverted cylindrical magnetrons shows that the conventional magnetron has a higher normalized growth rate. In contrast, the negative mass instability led to a significantly larger growth in the inverted geometry for smooth-bore magnetrons.

It appears that the dynamical behavior, which includes the negative/positive mass effects due to cylindrical geometries, and the intrinsic diocotron effects associated with the shear flow are strongly affected by the presence of SWS. Smooth-bore magnetrons are unlikely to achieve synchronism because of the constraint of $v(r_c) = 0$. This severely limits the velocity in the $E \times B$ drift.

ACKNOWLEDGMENTS

This paper is dedicated to the memory of Professor Ronald C. Davidson. This work was supported by Office of Naval Research Award Nos. N00014-13-1-0566 and N00014-16-1-2353, Air Force Office of Scientific Research Award No. FA9550-15-1-0097, and L-3 Communications Electron Device Division.

APPENDIX: JUMP CONDITION FOR CYLINDRICAL BRILLOUIN FLOW

The quantity $\phi'_{n1}(r_b)/\phi_{n1}(r_b)|_{r_{vac}}$ in Eq. (27) is given by[10]

$$\left.\frac{\phi'_{n1}}{\phi_{n1}}\right|_{r_{vac}} = \frac{\tilde{A}(r_{hub})}{\tilde{A}(r_{vac})}\left.\frac{\phi'_{n1}}{\phi_{n1}}\right|_{r_{hub}} + \frac{1}{r_b\tilde{A}(r_{vac})}\frac{\omega}{\Omega}\left[\left(\frac{\Omega}{\omega}-\frac{1}{\gamma_0^2}\right)\frac{1}{\omega_0}\left[\frac{\omega_0\xi(1+h)}{D\Delta}\right]\right]_{r_{hub}}, \tag{A.1}$$

where $r_{vac} = r_b + \epsilon$, $r_{hub} = r_b - \epsilon$, and $\epsilon \to 0$ (ϵ is positive for conventional magnetrons, negative for inverted). On the right-hand side of Eq. (A.1), $\phi'_{n1}/\phi_{n1}|_{r_{hub}}$ is obtained from the numerical solution to Eq. (14) of Ref. 19, for each spatial harmonic

$$r\frac{d}{dr}\left(r\tilde{A}\frac{d\phi}{dr}\right) + \tilde{C}\phi = 0, \tag{A.2}$$

where the functions $\tilde{A}$, $\tilde{C}$, D, Δ, Ω are defined. The equilibrium profile (density, velocity, and DC electric and magnetic field) for the relativistic cylindrical Brillouin flow[9,22,23] is used in Eq. (A.2).

[1]G. B. Collins, *Microwave Magnetrons* (McGraw-Hill, New York, 1948).
[2]L. Brillouin, "Theory of the magnetron. I," Phys. Rev. **60**(5), 385–396 (1941).
[3]J. C. Slater, *Microwave Electronics* (Van Nostrand, Princeton, NJ, 1950).
[4]A. Palevsky, G. Bekefi, and A. T. Drobot, "Numerical simulation of oscillating magnetrons," J. Appl. Phys. **52**(8), 4938–4941 (1981).
[5]P. J. Christenson and Y. Y. Lau, "One-dimensional modulational instability in a crossed-field gap," Phys. Rev. Lett. **76**(18), 3324–3327 (1996).
[6]P. J. Christenson, D. P. Chernin, A. L. Garner, and Y. Y. Lau, "Resistive destabilization of cycloidal electron flow and universality of (near-) Brillouin flow in a crossed-field gap," Phys. Plasmas **3**(12), 4455–4462 (1996).
[7]R. L. Walker, in *Microwave Magnetrons*, edited by G. B. Collins (McGraw-Hill, New York, 1948), p. 227.
[8]J. Benford, J. A. Swegle, and E. Schamiloglu, *High Power Microwaves*, 3rd ed. (CRC Press, Boca Raton, FL, 2015).
[9]Y. Y. Lau, J. W. Luginsland, K. L. Cartwright, D. H. Simon, W. Tang, B. W. Hoff, and R. M. Gilgenbach, "A re-examination of the Buneman–Hartree condition in a cylindrical smooth-bore relativistic magnetron," Phys. Plasmas **17**(3), 033102 (2010).
[10]D. H. Simon, Ph.D. Dissertation, The University of Michigan, Ann Arbor, 2016.
[11]O. Buneman, R. Levy, and L. Linson, "Stability of crossed-field electron beams," J. Appl. Phys. **37**(8), 3203 (1966).
[12]J. Swegle and E. Ott, "Instability of the Brillouin-flow equilibrium in magnetically insulated structures," Phys. Rev. Lett. **46**(14), 929–932 (1981).
[13]T. M. Antonsen, Jr., E. Ott, C. L. Chang, and A. T. Drobot, "Parametric scaling of the stability of relativistic laminar flow magnetic insulation," Phys. Fluids **28**(9), 2878–2881 (1985).
[14]R. Davidson, H. Chan, C. Chen, and S. Lund, "Equilibrium and stability properties of intense non-neutral electron flow," Rev. Mod. Phys. **63**(2), 341–374 (1991).
[15]R. C. Davidson, *Physics of Nonneutral Plasmas* (Imperial College Press, 2001).
[16]K. T. Tsang and R. C. Davidson, "Macroscopic cold-fluid equilibrium properties of relativistic non-neutral electron flow in a cylindrical diode," Phys. Rev. A **33**(6), 4284–4292 (1986).
[17]R. C. Davidson, K. T. Tsang, and H. S. Uhm, "Stabilization of diocotron instability by relativistic and electromagnetic effects for intense nonneutral electron flow," Phys. Lett. A **125**(1), 61–67 (1987).
[18]D. H. Simon, Y. Y. Lau, G. Greening, P. Wong, B. W. Hoff, and R. M. Gilgenbach, "Stability of Brillouin flow in planar, conventional, and inverted magnetrons," Phys. Plasmas **22**(8), 082104 (2015).
[19]D. Chernin and Y. Y. Lau, "Stability of laminar electron layers," Phys. Fluids **27**(9), 2319–2331 (1984).
[20]D. M. French, B. W. Hoff, Y. Y. Lau, and R. M. Gilgenbach, "Negative, positive, and infinite mass properties of a rotating electron beam," Appl. Phys. Lett. **97**(11), 111501 (2010).
[21]Y. Y. Lau, "Theory of crossed-field devices and a comparative study of other radiation sources," in *High-power Microwave Sources*, edited by V. L. Granatstein and I. Alexeff (Artech House, Norwood, MA, 1987), pp. 309–351.
[22]R. C. Davidson, G. L. Johnston, K. T. Tsang, and A. T. Drobot, "Cylindrical Brillouin flow in relativistic smooth-bore magnetrons," Proc. SPIE **1061**, 186–200 (1989).
[23]D. H. Simon, Y. Y. Lau, J. W. Luginsland, and R. M. Gilgenbach, "An unnoticed property of the cylindrical relativistic Brillouin flow," Phys. Plasmas **19**(4), 043103 (2012).
[24]R. M. Gilgenbach, Y. Y. Lau, D. M. French, B. W. Hoff, J. Luginsland, and M. Franzi, "Crossed field device," U.S. patent No. US8841867 B2 (23 Sep. 2014).
[25]R. M. Gilgenbach, Y. Y. Lau, D. M. French, B. W. Hoff, M. Franzi, and J. Luginsland, "Recirculating planar magnetrons for high-power high-frequency radiation generation," IEEE Trans. Plasma Sci. **39**(4), 980–987 (2011).
[26]M. A. Franzi, R. M. Gilgenbach, B. W. Hoff, D. A. Chalenski, D. Simon, Y. Y. Lau, and J. Luginsland, "Recirculating-planar-magnetron simulations and experiment," IEEE Trans. Plasma Sci. **41**(4), 639–645 (2013).
[27]J. W. Gewartowski and H. A. Watson, *Principles of Electron Tubes: Including Grid-Controlled Tubes, Microwave Tubes, and Gas Tubes* (Van Nostrand, Princeton, NJ, 1965).
[28]R. C. Davidson, K. Tsang, and J. A. Swegle, "Macroscopic extraordinary-mode stability properties of relativistic non-neutral electron flow in a planar diode with applied magnetic field," Phys. Fluids **27**(9), 2332–2345 (1984).
[29]N. M. Kroll and W. E. Lamb, "The resonant modes of the rising sun and other unstrapped magnetron anode blocks," J. Appl. Phys. **19**(2), 166–186 (1948).
[30]Y. Y. Lau and D. Chernin, "A review of the ac space-charge effect in electron–circuit interactions," Phys. Fluids B: Plasma Phys. **4**(11), 3473–3497 (1992).
[31]Y. Y. Lau and L. R. Barnett, "A low magnetic-field gyrotron gyro-magnetron," Int. J. Electron. **53**(6), 693–698 (1982).